Noble-transition metal nanoparticle breathing in a reactive gas atmosphere†

Valeri Petkov,[*a] Shiyao Shan,[b] Peter Chupas,[c] Jun Yin,[b] Lefu Yang,[b] Jin Luo[b] and Chuan-Jian Zhong[b]

In situ high-energy X-ray diffraction coupled to atomic pair distribution function analysis is used to obtain fundamental insight into the effect of the reactive gas environment on the atomic-scale structure of metallic particles less than 10 nm in size. To substantiate our recent discovery we investigate a wide range of noble-transition metal nanoparticles and confirm that they expand and contract radially when treated in oxidizing (O_2) and reducing (H_2) atmospheres, respectively. The results are confirmed by supplementary XAFS experiments. Using computer simulations guided by the experimental diffraction data we quantify the effect in terms of both relative lattice strain and absolute atomic displacements. In particular, we show that the effect leads to a small percent of extra surface strain corresponding to several tenths of Ångström displacements of the atoms at the outmost layer of the particles. The effect then gradually decays to zero within 4 atomic layers inside the particles. We also show that, reminiscent of a breathing type structural transformation, the effect is reproducible and reversible. We argue that because of its significance and widespread occurrence the effect should be taken into account in nanoparticle research.

Introduction

With current technology moving into smaller dimensions, metallic nanoparticles (NPs) are produced in increasing numbers and explored for various applications. The unique functionality of NPs stems from finite size effects that strongly impact their atomic-scale structure and, hence, properties. Also, NPs have a greatly increased surface to volume ratio and so they can interact strongly with their environment. Reactive gas environments have been shown to influence the surface chemistry[2] and shape[3] of metallic NPs but little is known about their influence on the overall atomic-scale structure. Revealing this influence is important since NPs are often post-synthesis treated and/or used in a reactive gas atmosphere.

Very recently[1] we investigated the effect of a reactive gas atmosphere on few noble (NM)–transition (TM) metal alloy NPs and discovered that they contract and expand radially when treated in oxidizing (O_2) and reducing (H_2) atmospheres,

respectively. However, fundamentals of the effect such as its origin, magnitude, NP chemistry dependence, range of spatial extent within the NPs and reproducibility remained unknown calling for further investigation. Here we report results from a study aimed at clarifying these fundamentals so that the effect is better understood and utilized. Following our recent investigation[1] the present study employs *in situ* high-energy X-ray diffraction (XRD) coupled to atomic pair distribution function (PDF) analysis. As we and others have repeatedly shown[4] this non-traditional experimental approach is very efficient in structural studies of nanosized materials, including metallic alloy NPs. Similar to other diffraction based techniques,[5,6] it yields data that can be used to test and refine structure models. From the models fine features of the atomic ordering in NPs can be discerned and well understood.[4,7]

Experimental

1.1 Sample preparation and characterization

To verify our discovery we expanded the class of NM–TM NPs to include single component, binary and ternary alloys, where NM = Pt, Au and TM = Co, Ni, Cu. Note that these NPs show not only diverse chemistry but also great potential for optical,[8] magnetic,[9] biomedical[10] and catalytic applications.[11–13] Also, exploring a wide range of NM–TM alloys is important since pure NMs are scarce and so are not amenable to large-scale applications. To conform to the requirements of real-life applications our synthesis effort targeted NPs less than 10 nm in size. The

[a] Department of Physics, Central Michigan University, Mt. Pleasant, Michigan 48859, USA. E-mail: petko1vg@cmich.edu; Fax: +1 989 774 2697; Tel: +1 989 774 3395

[b] Department of Chemistry, State University of New York at Binghamton, New York 13902, USA. E-mail: cjzhong@binghamton.edu; Fax: +1 607-777-4478; Tel: +1 607-777-4605

[c] X-ray Science Division, Advanced Photon Source, Argonne National Laboratory, Argonne, Illinois 60439, USA. E-mail: chupas@aps.anl.gov; Fax: +1 630-252-0365; Tel: +1 630-252-8651

† Electronic supplementary information (ESI) available: XRD patterns, TEM and catalytic activity data. See DOI: 10.1039/c3nr02582a

synthesis involved mixing of appropriate metal precursors in predefined ratios in solution.[14,15] Thiols/amines and oleic acid/oleylamine compounds were added to the synthesis solution as capping agents. Once cleaned from the synthesis solution, the NPs were mixed with carbon in a controlled ratio. The resulting suspension was dried in N_2. The NP loading on carbon was about 10–20 wt%.

The NP bulk composition was cross-checked by direct current plasma-atomic emission spectroscopy (DCP-AES) or inductively coupled plasma-optical emission spectroscopy (ICP-OES). For the measurements, the NP samples were dissolved in aqua regia, and then diluted to concentrations in the range of 1 to 50 ppm. Calibration curves were made from dissolved standards in the same acid matrix as the unknowns. Standards and unknowns were analyzed 10 times each resulting in <±2% error.

X-ray photoelectron spectroscopy (XPS) was used to determine the surface chemical composition of the NPs. XPS data were collected using a Physical Electronics Quantum 2000 Scanning ESCA Microprobe. This system uses a focused monochromatic Al Kα X-ray (1486.7 eV) source and a spherical section analyzer. X-ray beam with a diameter of 100 μm was rastered over a 1.3 mm by 0.2 mm rectangle on the samples. The incident X-ray beam was normal to the samples while the X-ray detector was at 45° away from the normal. The binding energy was calibrated using Cu $2p_{3/2}$ feature at 932.62 eV and Au $4f_{7/2}$ feature at 83.96 eV for known standards. During measurements samples experienced various degrees of charging. To minimize this, low energy electrons at ~1 eV, 20 μA and low energy Ar^+ ions were used. The percentages of the individual NM and TM species were determined from the relative composition analysis of the XPS peak areas.

The size and morphology of NPs was determined by transition electron microscopy (TEM) using a Hitachi H-7000 electron microscope (100 keV). For the TEM measurements NP samples were diluted in hexane and drop cast onto a carbon-coated copper grid followed by solvent evaporation in air at room temperature. HRTEM data were obtained on a JEOL JEM 2010 at an accelerator voltage of 200 keV. TEM results showed that the NPs studied here are highly monodisperse and with an average size of about 5.0(5) nm. Exemplary TEM and XPS data are shown in Fig. S1 and S2 of the ESI,† respectively.

X-ray absorption fine structure spectroscopy (XAFS) was used to determine particular metal–metal and metal–oxygen coordination environments as well as to cross-check the findings of XRD/PDF experiments for selected binary and ternary NM–TM alloys. *Ex situ* Pt L_3 edge (11 564 eV), Co K edge (7709 eV) and Ni K edge (8333 eV) XAFS spectra were collected on the bending magnet 9-BM-B line at the Advanced Photon Source, Argonne National Laboratory. To reduce higher order harmonics a double Si (111) monochromator was used along with a Rh-coated mirror. NP powder samples were pressed into pellets and measured in transmission geometry. Reference XANES spectra of Pt, Ni and Co metal foils were collected simultaneously for energy calibration. XAFS spectra can be divided into two regions: X-ray absorption near edge structure (XANES) and X-ray absorption fine structure (EXAFS). XANES and EXAFS spectra

were processed using software Athena and Artemis, respectively.[16] The fitting was limited to 2.0–12.0 $Å^{-1}$ for Pt L_3 edge, Ni and Co K edge spectra, using a Hanning window with dk = 1.0 $Å^{-1}$. The fits were performed in both the real and imaginary parts of $\chi(R)$ in the region 1.0 < R < 3.2 Å. Processing of XANES and EXAFS data is described in more detail in our previous studies.[15a,b,17] Exemplary EXAFS and XANES spectra and metal–metal and metal–oxygen coordination numbers and distances extracted from them are shown in Fig. S3–S5, and Tables S1 and S2 in the ESI.†

1.2 XRD experiments

In situ high-energy XRD data were collected at the beam line 11-ID-B, at the Advanced Photon Source, Argonne National Laboratory, using X-rays of energy 90.48 keV (λ = 0.1372 Å). A sample cell described in ref. 18 was employed. To improve the XRD data statistics, a large area detector was employed. The diffracted intensities were reduced to structure functions defined as

$$S(q) = 1 + [I^{coh\cdot}(q) - \sum c_i|f_i(q)|^2]/|\sum c_i f_i(q)|^2, \tag{1}$$

where c_i and $f_i(q)$ are the atomic concentration and X-ray scattering factor respectively for the atomic species of type i. The structure factors were Fourier transformed into atomic PDFs[4] as follows:

$$G(r) = \frac{2}{\pi} \int_{q=0}^{q_{max}} q[S(q) - 1]\sin(qr)dq \tag{2}$$

where q is the magnitude of the wave vector ($q = 4\pi\sin\theta/\lambda$), 2θ is the angle between the incoming and outgoing X-rays and λ is the wavelength of the X-rays used. The so obtained PDF $G(r)$ gives the number of atoms in a spherical shell of unit thickness at a radial distance r from a reference atom. It peaks at distances corresponding to the radii of the atomic coordination spheres in materials, starting from the first one (see Fig. S6 in the ESI†). A particular feature of the atomic PDF analysis is that it uses both the Bragg-like peaks and the diffuse scattering components in the XRD pattern. In this way both the existing atomic order, manifested in the Bragg-like peaks, and all structural "imperfections" that are responsible for its limited extent, manifested in the diffuse component of the XRD pattern, are reflected in the experimental PDFs. This renders atomic PDF analyses very well suited to study nanosized materials which show rather diffuse XRD patterns (see Fig. 1) because the periodicity in the atomic ordering is substantially limited by NP size and surface relaxation effects.[4]

1.3 Structure modeling

In this study we used two distinct structure modeling approaches. At first the experimental PDF data were approached with models based on crystalline lattices. In this type of modeling a PDF for an infinite crystalline lattice is first computed. Then each of the coordination spheres of the perfect lattice is broadened by a convolution with a Gaussian function to take into account the presence of thermal (Debye–Waller
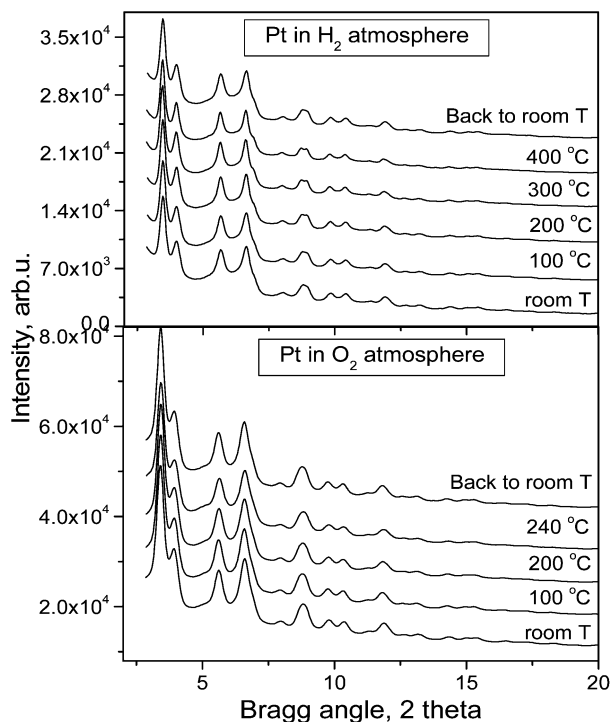
Fig. 1 Experimental XRD patterns for Pt NPs thermally treated in O_2 and H_2 atmospheres. Note that the high-energy XRD patterns and their Fourier counterparts, the atomic PDFs, reflect assembly averaged structural features of all NPs sampled by the X-ray beam in a way traditional powder XRD represents an assembly average of all polycrystallites sampled by the X-ray beam in those experiments. Comparing particle's assembly averaged structural features to particle's assembly averaged properties (e.g., catalytic) puts structure–property relationship exploration on the same footing.

type) and static local atomic displacements in NPs. At the same time the computed PDF is multiplied by a particle shape (spherical in our case) dependent function which is zero for distances longer than the size of the NPs being modeled. It is a simplistic approximation to the structure of real NPs but is useful since it allows (i) the type of their atomic ordering to be verified and (ii) a set of structural parameters (e.g., lattice constants) to be obtained that may be used to distinguish between different NPs. The calculations were done with the help of the program PDFgui.[19] Data from literature sources for the face-centered cubic (fcc)-type lattices occurring in bulk NMs and TMs were used as starting values in the NP structure modeling. It was done as to minimize a goodness-of-fit indicator, R_w, defined as:

$$R_w = \left\{ \frac{\sum w_i \left(G_i^{\text{exp.}} - G_i^{\text{calc.}} \right)^2}{\sum w_i \left(G_i^{\text{exp.}} \right)^2} \right\}^{1/2} \qquad (3)$$

where $G^{\text{exp.}}$ and $G^{\text{calc.}}$ are the experimental and calculated PDFs, respectively, and w_i are the weighting factors reflecting the statistical quality of the individual data points.

We also employed reverse Monte Carlo simulations.[20] In contrast to the crystalline-lattice constrained modeling, RMC simulations do not imply any structure uniformity and periodicity and so can yield a more unbiased, i.e. not crystalline-lattice

averaged out, picture of the overall atomic ordering in NPs. A finite size atomic configuration cut out from a perfect fcc-lattice was used as an initial step in the modeling. The configuration was spherical in shape and about 5 nm in diameter i.e. with a size and shape similar to those of the NPs studied here. As an example the starting configuration used in the RMC simulation of Pt NPs is shown in Fig. S7 in the ESI.† In the simulations the position of each atom from the approximately 5000 atom configuration was adjusted as to minimize the difference R_w (see eqn (3) above) between the model and respective experimental PDF data. Atoms were constrained (i) not to come closer than pre-selected distances and (ii) to maintain as maximal (i.e. as close to 12) as possible coordination numbers. The first constraint reflects the fact that atoms in the NPs do not approach each other closer than distances equal to the sum of the respective atomic radii. The second constraint takes into account the close packing nature of the fcc-type atomic ordering in NMs and NM–TM alloys. At the same time the energy of the configuration was optimized by minimizing pair-wise (Lennard-Jones type) potential taken from literature sources.[21] The simulations were done with the help of a new version of the program RMC++ (ref. 22) expanding on our recent work published in ref. 7.

Results and discussion

Often as-synthesized NPs are subjected to thermal treatment in a gas atmosphere to remove the organic molecules capping their surface and only then used in various applications. We conducted in situ high-energy XRD experiments following two standard treatment protocols, namely, thermal treatment in an oxidizing (80 vol% N_2 + 20 vol% O_2) atmosphere at 240 °C and in a reducing (97 vol % N_2 + 3 vol % H_2) atmosphere at 400 °C.

As an example experimental high-energy XRD patterns for Pt NPs are shown in Fig. 1. The XRD patterns exhibit very broad diffraction peaks, a picture typical for nanosized materials. The peak shape and width do not change significantly when the samples are thermally treated in an O_2 or H_2 atmosphere indicating no significant change in the NP morphology and size. No new diffraction features appear either, indicating no formation of new bulk nanophases. The very diffuse character of the Bragg peaks, however, makes it difficult to reveal the exact nature and magnitude of the structural changes in the NPs exposed to different reactive gas atmospheres. To ease the difficulty, the XRD data were reduced to their Fourier counterparts, i.e. to the respective atomic PDFs.[4]
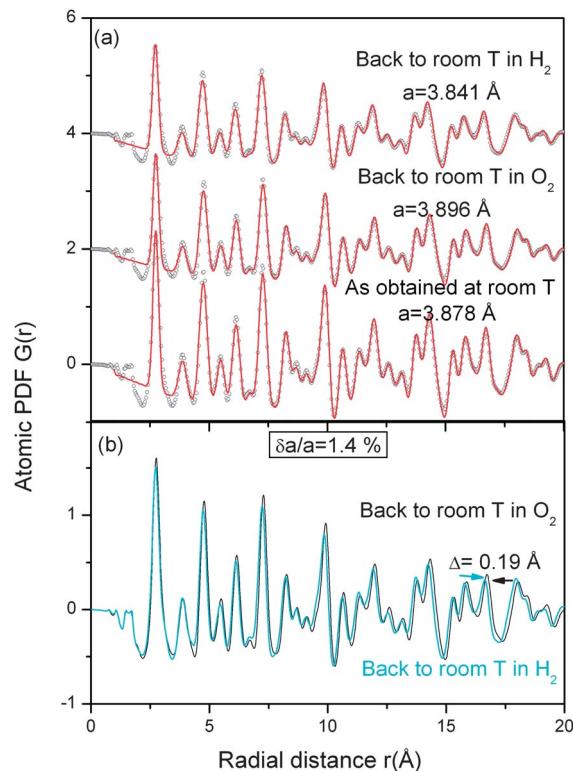
Atomic PDFs for pure Pt NPs treated in oxidizing and reducing atmospheres and then cooled down to room temperature are shown in Fig. 2. The PDFs exhibit a series of well-defined peaks reflecting the well defined sequence of coordination spheres in the Pt NPs studied here. The PDFs were approached with a model featuring a fcc-type lattice that occurs in bulk Pt. As can be seen in Fig. 2a, the experimental PDFs are well reproduced by a fcc-type of model. The result shows that as-obtained and treated Pt NPs exhibit the structure type of their bulk counterpart. No detectable amount of bulk metal oxides or hydride nanophases is revealed by the PDF analysis, either. The
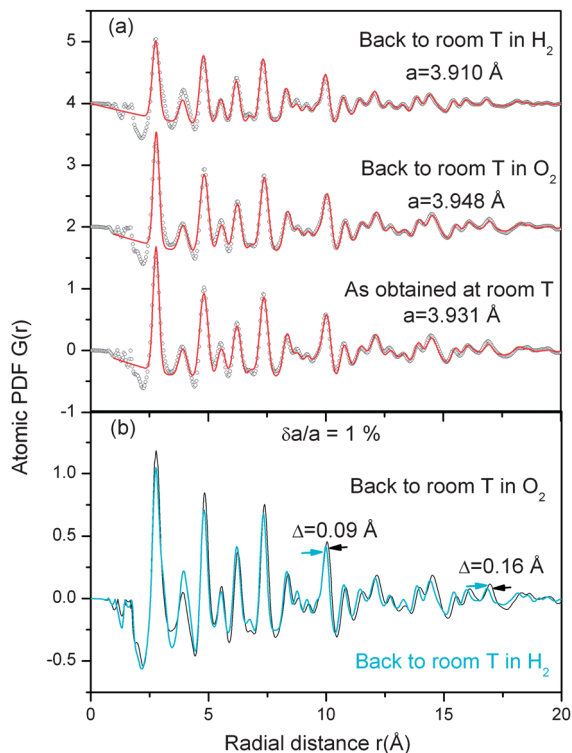
Fig. 2 Low-r part of the experimental (symbols) and fcc-model (solid line) atomic PDFs for as-obtained Pt NPs and for Pt NPs that have been thermally treated in O_2 and H_2 atmospheres, and then cooled down to room temperature (a). The refined fcc-lattice parameters are given by each dataset. In (b), the experimental PDFs for NPs treated in O_2 and H_2 atmospheres are compared to emphasize their different structural states.

Fig. 3 Low-r part of the experimental (symbols) and model (solid line) atomic PDFs for as-obtained $Pt_{45}Co_{55}$ NPs and NPs that have been thermally treated in O_2 and H_2 atmospheres, and then cooled down to room temperature (a). The refined fcc-lattice parameters are given by each dataset. In (b), the experimental PDFs for NPs treated in O_2 and H_2 atmospheres are compared to emphasize their different structural states.

parameter of the respective fcc lattices is considerably changed. It increases from 3.931(1) Å to 3.948(1) Å with the Pt NPs exposed to an O_2 atmosphere indicating that they expand. On the other hand, it decreases to 3.910(1) Å with the Pt NPs exposed to a H_2 atmosphere indicating that they contract. The expansion/contraction is such that the atomic coordination spheres/PDF peaks remain well defined and only shifted with respect to each other (see Fig. 2b), with the shift increasing with the interatomic distances (see Fig. 2b for the evolution of the shift, Δ, with the interatomic distances). When measured in terms of the change, $\delta a/a$, in the parameter of the fcc-type lattice the effect amounts to about 1%. Here δa is the difference between the lattice parameters of the Pt NPs treated in O_2 and H_2 atmospheres, respectively, and a is the lattice parameter of the as-obtained Pt NPs. Since the lattice parameters are obtained through a whole profile fit to experimental PDFs using a model assuming a structure uniformity and perfect lattice periodicity the quantity $\delta a/a$ represents the relative change in the positions of all atomic coordination spheres in Pt NPs, from the first to the most distant one.

Adding a second element to the NPs, *i.e.* considering Pt-based binary alloys, does not change the overall picture. Experimental atomic PDFs for as-obtained $Pt_{45}Co_{55}$ NPs and NPs thermally treated in O_2 and H_2 atmospheres are shown in Fig. 3. The respective experimental XRD patterns are shown in

Fig. S8 of the ESI.† Similar to the case of Pt NPs, the atomic ordering in as-obtained $Pt_{45}Co_{55}$ NPs can be well approximated with a model featuring a single nanophase of a fcc-type structure. The lattice parameter of this nanophase is 3.878(1) Å. It is shorter than that of pure Pt NPs (3.931(1) Å) because of the mixing of Pt with Co species that have a considerably smaller atomic dimension ($d_{Pt} = 1.39$ Å *vs.* $d_{Co} = 1.25$ Å). $Pt_{45}Co_{55}$ NPs remain a single nanophase when they are thermally treated in O_2 and H_2 atmospheres. For the NPs exposed to O_2 the fcc lattice parameter increases to 3.896(1) Å. For those exposed to H_2 it decreases to 3.841(1) Å. Here the relative change, $\delta a/a$, in the parameter of the fcc-type lattices, and, respectively, in the interatomic distances in the oxidized and reduced samples, is about 1.4%. The result is in line with the findings of XAFS experiments (see Table S2 in the ESI†) showing that the first neighbor Pt–Pt distances in Pt-based binary alloys subjected to a treatment in a reducing atmosphere shrink from 2.73 Å to 2.69 Å, *i.e.* shrink by about 1.4%. Note that the effect is cumulative and amounts to 0.19 Å at interatomic distances of approximately 16 Å, as directly measured from the experimental PDF data (see Fig. 3b).

As an example of ternary alloys we investigated $Pt_{50}Co_{25}Ni_{25}$ NPs. Their XRD patterns are shown in Fig. S9 of the ESI.† Here the lattice parameter of the as-obtained alloy NPs is 3.813(1) Å. When thermally treated in O_2 and H_2 atmospheres and then

cooled down to room temperature the NPs retain their fcc-type structure, as shown by the fits in Fig. 4a, but expand and contract, respectively. The opposite directions of the structural changes in the NPs treated in the two different gas atmospheres can be revealed straightforwardly by examining the position of the first PDF peak/coordination sphere in $Pt_{50}Co_{25}Ni_{25}$ NPs. It is at 2.690(1) Å for the untreated sample, at 2.730(1) Å for that exposed to O_2 and at 2.650(1) Å for the H_2 treated sample. The respective lattice parameters are 3.813(1) Å, 3.862(1) Å and 3.750(1) Å. The relative change, $\delta a/a$, in the lattice parameter of the oxidized and reduced samples is about 3%. The result is in line with the findings of XAFS experiments (see Table S1 in the ESI†) showing a 3% shrinkage in the first neighbor Pt–Pt and TM–TM distances in Pt–TM ternary alloys subjected to a treatment in a reducing atmosphere. The effect is cumulative amounting to 0.39 Å at interatomic distances of about 16 Å (see Fig. 4b).

For completeness we also studied NPs that do not contain Pt. Experimental atomic PDFs for carbon supported $Au_{50}Cu_{50}$ NPs thermally treated in O_2 and H_2 atmospheres are shown in Fig. S10.† Here the thermally treated NPs appear with an improved degree of crystallinity yet expand and contract, respectively. The relative change, $\delta a/a$, in the fcc-lattice parameter of the oxidized and reduced samples was found to be about 3.6%.
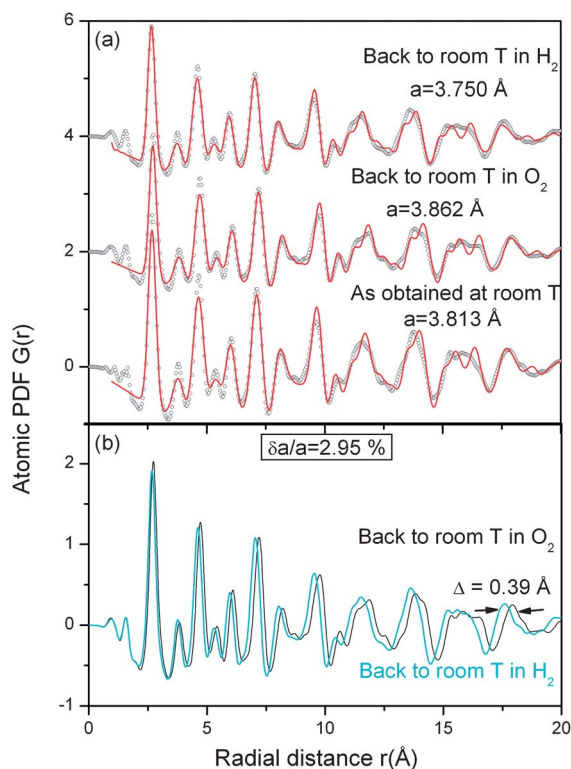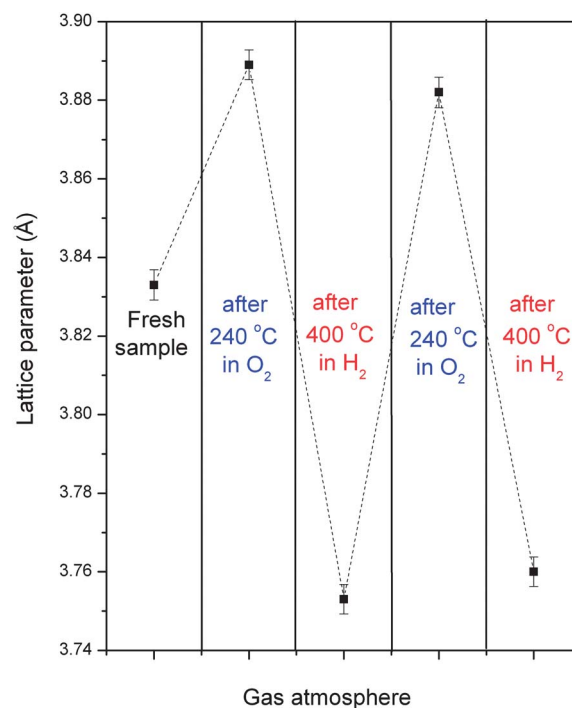
Next we explored the reproducibility of the effect starting with fresh $Pt_{25}Ni_{16}Co_{59}$ NPs having a fcc-lattice parameter of 3.833(1) Å (see Fig. 5). When treated in an oxidizing atmosphere the NPs expanded and their lattice parameter increased to 3.887(1) Å. A subsequent treatment in a reducing atmosphere contracted the NPs leading to a decrease of the lattice parameter to a value of 3.750(1) Å. Repeating the sequence of treatments made the NPs oscillate between their expanded and contracted structural states, differing by $\delta a/a = 3.5\%$, in a breathing-like manner. The experiment showed that the effect is largely reproducible and reversible in character.

The consistency of NPs restructuring with changing the reactive gas atmosphere over a variety of NM–TM systems, from single component to ternary alloys, shows that the effect is due to a physico-chemical process common to all NPs. Reversible expansion or contraction of interatomic distances is a process common to any material exposed to changes in temperature. Thermal expansion/contraction, however, scales with the temperature changes while the expanded/contracted structural states of NPs observed here remain stable when the NPs are brought back to room temperature and taken out of the respective gas atmosphere. Besides, the effect of thermal expansion/contraction on the atomic-scale structure is only about $\delta a/a = 0.2$–0.4% (ref. 23) in the temperature range covered by our studies, i.e. it is not strong enough to explain the $\delta a/a$ values of a small percent we observe.

Rearrangement of atomic species due to chemical disordering/ordering is common to NM–TM alloys and can lead to expansion/contraction of the interatomic distances. The effect

Fig. 4 Low-r part of the experimental (symbols) and model (solid line) atomic PDFs for as-obtained $Pt_{50}Co_{25}Ni_{25}$ NPs and NPs that have been thermally treated in O_2 and H_2 atmospheres, and then cooled down to room temperature (a). The refined fcc-lattice parameters are given by each dataset. In (b), the experimental PDFs for NPs treated in O_2 and H_2 atmospheres are compared to emphasize their different structural states.


Fig. 5 Evolution of the fcc-lattice parameter of $Pt_{25}Ni_{16}Co_{59}$ NPs thermally treated in O_2 (at 240 °C) and H_2 (at 400 °C) atmospheres, as denoted on the horizontal axis, and then cooled down to room temperature.

amounts to $\delta a/a = 0.2–0.3\%$ (ref. 24) and does not operate in single component systems such as Pt NPs where we find a relative change of $\delta a/a = 1\%$. On the other hand, as shown by our XPS and XAFS studies (see Fig. S2 and Tables S1 and S2 in the ESI†), the metal species in NM–TM NPs exhibit some rearrangement with a change in the reactive gas atmosphere. Therefore, changes in the chemical ordering, *i.e.* rearrangement of the NM and TM species, may not be completely ruled out as a contributor to the breathing-type restructuring in the alloy NPs observed here.

Another process common to all NPs is their interaction with the reactive gas atmosphere. Metal-oxide-like and chemisorbed oxygen species will develop on the very top surface of NPs exposed to O_2 (ref. 25–28) (also see Tables S1 and S2 in the ESI†). Our XRD, XPS and XAFS experiments are not sensitive enough to reveal if these species entirely cover the NP surface or form extended islands on it. In either case the incommensurate lattices of the metal NPs and the oxygenated surface (*e.g.* see Table S3 in the ESI†) would lead to tensile stresses[28] orthogonal to the NPs' surface. These extra stresses will have to be accommodated by the NPs' interior[29] eventually causing the NP to expand radially. Treatment in a H_2 atmosphere largely removes the oxygenated species from the NP surface (*e.g.* see Tables S1 and S2 in the ESI†) and so relieves it from the extra tensile stress. Furthermore, due to their very different electronegativity values (2.2 for H_2 *vs.* 3.4 for O_2), adsorbed hydrogen gas species will interact, including energy of binding and charge transfer,[30] very differently with the NPs. The different interactions may propagate well into the NPs' interior eventually making the NP contract radially. Note, although rare, cases of bulk metals contracting when treated in a hydrogen atmosphere are known. The phenomenon is explained in terms of electronegativity effects[31] and may be more common in metals and alloys confined to nanoscale dimensions.

To understand the nature of the interactions of oxygen and hydrogen species with NM–TM NPs in finer detail we constructed a real size (5 nm) and shape (spherical) structure model for Pt NPs employing reverse Monte Carlo simulations as described in Section 1.3. The RMC constructed models reproduce very well the experimental PDFs (see Fig. 6b) for O_2 and H_2 treated NPs, including the shift in the positions of the respective atomic coordination spheres (compare the data in Fig. 3b and 6a). Analysis of the models (see Fig. 7) shows that not all but only the top 3–4 layers in the Pt NPs treated in H_2 are considerably contracted when compared to the same layers in the Pt NPs treated in an O_2 atmosphere. In particular, atoms from the very top layer of the H_2 treated NPs are displaced, on average, by as much as 0.31(2) Å in a direction towards the NP centre. The magnitude of the displacements gradually decays inside the NPs becoming nearly zero in the forth atomic layer (*i.e.* at approx. 8–10 Å) beneath the NP surface. The result is consistent with our recent DFT studies[32] showing that the effect of adsorbed species is mostly confined to the surface region of metallic NPs.

Elasticity theory predicts[33] and studies have shown[5,34] that surface stresses die off inside NPs with a decay length of approximately $(1/2\pi)L$, where L is the NP size. With $L \sim 5$ nm, it may be expected the reactive gas induced surface stress to decay
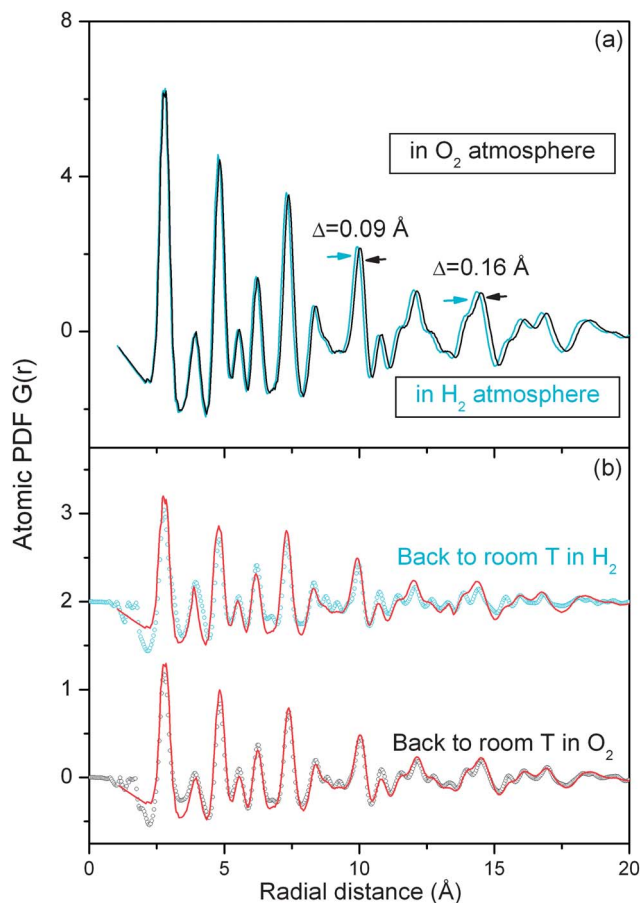
Fig. 6 Experimental (symbols) and RMC fit (line) atomic PDFs for Pt NPs treated in O_2 and H_2 atmospheres (b). Comparison between the RMC fit PDFs demonstrating the shift in the respective atomic coordination sphere (a).

within a depth of 8 Å, in good agreement with the findings of the RMC simulations. If an atom at the NP center is selected as a reference point of the experimental PDFs (see Fig. S6 in the
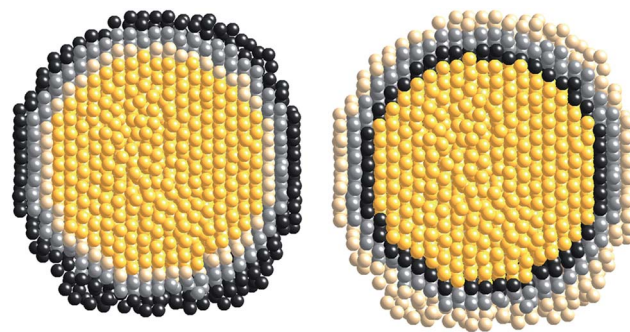
Fig. 7 Models for 5 nm Pt NPs treated in H_2 (left) and O_2 (right) atmospheres as refined against the respective experimental PDF data *via* reverse Monte Carlo simulations. The models are averaged over several configurations resulting from different runs of the simulations. The configurations differ in minor details such as coordinates of the individual atoms but are statistically indistinguishable sharing the same major structural feature. That is, the top 3–4 atomic layers in the model for H_2 treated NPs (left) are considerably contracted when compared to the same layers in the NPs treated in O_2 (right). Different color codes are used for the top surface layers of the samples treated in H_2 and O_2 atmospheres to underline the different impact of the different reactive gases on the NPs' atomic-scale structure.

ESI†) and the relative change $\delta a/a = 1\%$ in the interatomic distances obtained by the fcc-lattice based model is used, it can be predicted that the very top atomic layer of 5 nm Pt NPs treated in a H_2 atmosphere is contracted, when compared to the case of an O_2 atmosphere, by about 0.25 Å. This value is close to but smaller than the RMC findings. The reason is that it comes from a model featuring a uniform contraction of a periodic fcc lattice while real NPs are not quite uniform especially close to their surface where, due to the breaking of the periodicity in the atomic ordering, larger structural variations are more likely to occur. Therefore, the predictions of the fcc-lattice based models can be viewed at as a low-limit approximation of the actual magnitude of the breathing-type restructuring of the surface layers in NPs treated in a reactive gas atmosphere.

Within the limits of this approximation, it may be predicted that the top layer in $Pt_{45}Co_{55}$ NPs treated in H_2 ($\delta a/a = 1.4\%$) is contracted radially by at least 0.35(2) Å while the top layer in $Pt_{50}Co_{25}Ni_{25}$ NPs treated in H_2 ($\delta a/a = 3\%$) – by at least 0.75(2) Å. Looking at these results it may be safely assumed that in the case of alloy NPs (*e.g.* ternary $Pt_{50}Co_{25}Ni_{25}$ with $\delta a/a = 3\%$) the surface restructuring may be facilitated by the different size and chemistry of the particular NM and TM species involved and so it may appear with an increased magnitude when compared to the case of single component NPs (*e.g.* Pt with $\delta a/a = 1\%$). Also, the reactive gas induced surface restructuring may appear with a different magnitude in different alloy NPs because of the different electronic interactions between the respective NM and TM species.[35] For example, Au–Cu alloys are known to accommodate more strain than other NM–TM alloys[35,36] which may explain the rather large magnitude ($\delta a/a \sim 3.6\%$) of the surface strain observed with $Au_{50}Cu_{50}$ NPs when compared to the case of $Pt_{45}Co_{55}$ NPs.

Radial contraction is not uncommon in NPs less than 10 nm in size. For example, coherent XRD experiments[5] have found that, due to finite size effects, the top 1–2 layers in 4 nm Au NPs are permanently contracted by $\sim$0.2 Å. The reactive gas atmosphere induced contraction in alloy NPs we observe is (i) considerably stronger and (ii) reversible in character.

The contraction of the 3–4 top surface layers in NPs treated in H_2 concurs with a large increase in their catalytic activity. For example, with the H_2 treated $Pt_{25}Ni_{16}Co_{59}$ NPs, the gas phase CO conversion rate increases by $\sim$10 times, and the mass activity for electrocatalytic oxygen reduction reaction (ORR) increases by $\sim$4 times (see Fig. S11 and S12 in the ESI†). A similar increase in the catalytic activity is observed with the other NM–TM NPs studied here (*e.g.*, see Fig. S13†). The results are fully consistent with theoretical predictions that only a small (1–3%) percent of compressive strain on the NP surface is enough to decrease the energy of d-band electrons with respect to the Fermi level and so lower the binding energy of the CO species to the NP surface, substantially improving the catalytic activity.[37] The results, *i.e.* the appearance of a small % of compressive strain, are also in line with the optimization of the binding energy of O_2 on alloy NPs which consequently increases the electrocatalytic activity for ORR.[38]

The effect of reactive gas species on the atomic-scale structure of metallic NPs of diverse chemistry is not easy to predict theoretically. It may not be automatically assumed from the behavior of the respective bulk counterparts either. For example, studies on single crystals of Pt have shown that both O_2 and H_2 induce compressive surface stresses[39] while, as our studies show, Pt NPs expand and contract, respectively. Being a volume sensitive technique high-energy XRD coupled to atomic PDF analysis is hardly sensitive to the type of gas species adsorbed on the NP surface[25] but, contrary to the common belief, is sensitive to the effect of those species on the NPs' overall atomic-scale structure. The reason is that (i) the effect is significant and (ii) involves 3–4 top surface layers which constitute a substantial part of the volume of NPs less than 10 nm in size. This makes it possible for *in situ* high-energy XRD coupled to atomic PDF analysis to open a new window into how reactive gasses interact with metallic NPs. By approaching experimental PDF data with not entirely realistic but easy to apply crystalline lattice based models very reasonable estimates for the character (*e.g.* expansion or contraction) and magnitude of the surface reconstruction of NPs treated in a reactive gas atmosphere can be obtained. When more strict but complicated 3D modeling techniques such as RMC and molecular dynamics are employed much more precise estimates can be obtained. These estimates may help in explaining why NPs treated in reactive gas atmospheres behave one way or another. If a deeper understanding is needed, the refined 3D structure models may serve as a basis for computing and predicting NP properties of interest.

Conclusions

The interaction of reactive gases with NPs is rather dynamic in character and may involve considerable rearrangement of the atomic species close to the NP surface.[1,2] The present study provides evidence that the overall effect of this interaction may also bring NM–TM NPs to structural states that persist even after the NPs are taken out of the respective gas atmosphere and brought back to room temperature. That is, NPs treated in an oxidizing (O_2) atmosphere may expand while those treated in a reducing (H_2) atmosphere contract significantly. The gas induced contraction/expansion depends on NP chemistry and may (*e.g.* alloy NPs) or may not (*e.g.* single component NPs) involve chemical ordering/disordering effects. According to our study, the gas species induced extra surface strain has the following characteristics: (i) it is observed not only with alloys but also with single component NPs, (ii) it may appear stronger with the former compared to the latter due to rearrangement of NM and TM species with respect to each other and/or electronic effects acting when NM and TM species are mixed together, (iii) it is confined to the 3–4 top surface layers of NPs, (iv) it is not due to common thermal expansion/contraction but likely has its roots in the different electronegativity of the different adsorbed gas species, (v) it is reproducible and reversible following changes in the gas atmosphere, and (vi) it is significant rendering the interatomic distances between the surface NP atoms in the compressed and expanded structural states differ by several tenths of Ångströms. As a result, it may affect the NP properties. For example, the compressed structural state

of NM–TM NPs is, at the least, more favorable for certain catalytic reactions than the expanded one. Given the fact that about 30 to 70% of all atoms in less than 10 nm in size NPs reside on their 3–4 top surface layers, the substantial increase or decrease in the interatomic distances within these layers may also affect the NPs' optical and magnetic properties.[40,41] Therefore, the particular reactive gas environment should be accounted for in NP research. Moreover, when recognized, it may prove to be a helpful parameter for fine tuning NPs' functionality. In particular, by changing the reactive gas atmosphere desired structural states of NPs may be induced selectively and repeatedly opening new avenues for the design of useful nanodevices. Indeed the first reactive gas driven, metallic NP-based device is already a fact.[42] More applications could be just around the corner.

Acknowledgements

References

1 V. Petkov, L. Yang, J. Yin, S. Shan, B. Wanjala, J. Luo, K. W. Chapman and C. J. Zhong, *Phys. Rev. Lett.*, 2012, **109**, 125504.

2 F. Tao, M. E. Grass, Y. Zhang, D. R. Butcher, J. R. Renzas, Zh. Liu, J. Y. Chung, B. S. Mun, M. Salmeron and G. A. Somorjai, *Science*, 2008, **322**, 832; F. Tao, M. E. Grass, Y. Zhang, D. R. Butcher, F. Aksoy, S. Aloni, V. Altoe, S. Alayoglu, J. R. Renzas, Ch.-K. Tsung, Z. Zhu, Z. Liu, M. Salmeron and G. A. Somorjai, *J. Am. Chem. Soc.*, 2010, **132**, 8697.

3 P. L. Hansen, J. B. Wagner, S. Helveg, J. R. Rostup-Nielsen, B. S. Clausen and B. S. H. Topsoe, *Science*, 2002, **295**, 2053–2055.

4 T. Egami and S. J. L. Billinge, in *Underneath the Bragg Peaks*, Pergamon, Amsterdam, 2003; V. Petkov, *Mater. Today*, 2008, **11**, 28; Th. Proffen, V. Petkov, S. J. L. Billinge and T. Vogt, *Z. Kristallogr.*, 2002, **217**, 47; V. Petkov, R. Loukrakpam, L. Yang, B. N. Wanjala, J. Luo, C. J. Zhong and S. Shastri, *Nano Lett.*, 2012, **12**, 4289; V. Petkov, T. Ohta, Y. Hou and Y. Ren, *J. Phys. Chem. C*, 2007, **111**, 714.

5 W. J. Huang, R. Sun, L. Tao, L. D. Menard, R. J. Nuzzo and J. M. Zou, *Nat. Mater.*, 2008, **7**, 308.

6 P. D. Jadzinsky, G. Galero, C. J. Akerson, D. A. Bushnell and R. D. Kornberg, *Science*, 2007, **318**, 430.

7 V. Petkov, I. Moreels, Z. Hens and Y. Ren, *Phys. Rev. B: Condens. Matter Mater. Phys.*, 2010, **81**, 241304.

8 P. Mulvaney, *Langmuir*, 1996, **12**, 788.

9 D. Alloyeau, C. Ricolleau, C. Mottet, T. Oitkawa, C. Langlois, Y. Le Bouar, N. Braidy and A. Loiseau, *Nat. Mater.*, 2009, **8**, 940.

10 Ch.-An. J. Lin, Ch.-H. Lee, J.-T. Hsiech, H. H. Wang, J. K. Li, J. L. Shen, W. H. Chan, H.-I. Yeh and W. H. Chang, *Jpn. J. Med. Electron. Biol. Eng.*, 2009, **29**, 276.

11 G. A. Samorjai, in *Introduction to Surface Chemistry and Catalysis*, Wiley, New York, 1994.

12 D. I. Enache, J. K. Edwards, P. Landon, B. Solsona-Espriu, A. F. Carley, A. A. Herzing, M. Watanabe, C. J. Kiely, D. W. Knight and G. J. Hutchings, *Science*, 2006, **311**, 362.

13 J. K. Norskov and C. H. Christensen, *Science*, 2006, **312**, 1322.

14 B. N. Wanjala, B. Fang, R. Loukrakpam, Y. Chen, M. Engelhard, J. Luo, J. Yin, L. Yang, S. Shan and C. J. Zhong, *ACS Catal.*, 2012, **2**, 795.

15 (*a*) B. Wanjala, R. Loukrakpam, J. Luo, P. N. Njoki, D. Mott, M. Shao, L. Protsailo, T. Kawamura and C. J. Zhong, *J. Phys. Chem. C*, 2010, **114**, 17580; (*b*) R. Loukrakpam, J. Luo, T. He, Y. Chen, Z. Xu, P. N. Njoki, B. N. Wangala, B. Fang, D. Mott, J. Yin, J. Klar, B. Powell and C. J. Zhong, *J. Phys. Chem. C*, 2011, **115**, 1682.

16 B. Ravel and M. Newville, *J. Synchrotron Radiat.*, 2005, **12**, 537.

17 R. Loukrakpam, B. N. wanjala, J. Yin, B. fang, J. Luo, Y. Chen, V. Petkov, C. J. Zhong, M. Shao, L. protsailo and T. Kawamura, *ACS Catal.*, 2011, **1**, 562; B. fang, J. Luo, Y. Chen, B. N. wanjala, R. Loukrakpam, J. Hong, J. Yin, X. Hu, P. Hu and C. J. Zhong, *ChemCatChem*, 2011, **3**, 583.

18 P. J. Chupas, K. W. Chapman, Ch. Kurtz, J. C. Hanson, P. Lee and C. P. Grey, *J. Appl. Crystallogr.*, 2008, **41**, 822; S. M. Oxford, P. L. Lee, P. J. Chupas, K. W. Chapman, M. C. Kung and H. Kun, *J. Phys. Chem. C*, 2010, **114**, 17085.

19 C. L. Farrow, P. Juhás, J. W. Liu, D. E. Bryndin, E. Božin, J. Bloch, Th. Proffen and S. J. Billinge, *J. Phys.: Condens. Matter*, 2007, **19**, 335219.

20 R. L. McGreevy and L. Pusztai, *Mol. Simul.*, 1998, **1**, 359.

21 H. Heinz, R. A. Vaia, B. I. Farmer and R. R. Naik, *J. Phys. Chem. C*, 2008, **112**, 1728190.

22 O. Gereben, P. Jovari, L. Temleitner and L. Pusztai, *J. Optoelectron. Adv. Mater.*, 2007, **9**, 3021.

23 J. W. Arblaster, *Platinum Met. Rev.*, 1997, **41**, 12; *CRC Handbook of Chemistry and Physics*, ed. R. R. Lide, CRC Press, Boca Raton, Florida, 2003.

24 M. L. Bhatia and R. W. Cahn, *Intermetallics*, 2005, **13**, 474.

25 M. A. Newton, K. W. Chapman, D. Thompsett and P. J. Chupas, *J. Am. Chem. Soc.*, 2012, **134**, 5036.

26 D. R. Butcher, M. E. Grass, Zh. Zeng, F. Aksoy, H. Bluhm, W.-H. Li, B. S. Mun, G. A. Somorjai and Z. Liu, *J. Am. Chem. Soc.*, 2011, **133**, 20319.

27 B. L. M. Hendriksen and J. M. W. Frenken, *Phys. Rev. Lett.*, 2002, **89**, 046101.

28 L. Yang, S. Shan, R. Loukrakpam, V. Petkov, Y. Ren, B. N. Wanjala, M. H. Engelhard, J. Luo, J. Yin, Y. Chen and C. J. Zhong, *J. Am. Chem. Soc.*, 2012, **134**, 15048.

29 Q. Jiang, L. H. Liang and D. S. Zhao, *J. Phys. Chem. B*, 2001, **105**, 6275.

30 C. M. Varma and A. J. Wilson, *Phys. Rev. B: Condens. Matter Mater. Phys.*, 1980, **22**, 3795.

31 K. KKurosaki, D. Setoyama, J. Matsunaga, H. Muta, K. KKurosaki, M. Uno and Sh. Yamanaka, *J. Alloys Compd.*, 2006, **426**, 67.

32 M. Welborn, W. Tang, J. Ryu, R. M. Crooks, V. Petkov and G. Henkelman, *J. Chem. Phys.*, 2011, **135**, 014503.

33 L. D. Landay and E. M. Lifshitz, in *Theory of Elasticity*, Pergamon Pres, Oxford, 1986.

34 R. Harder, M. A. Pfeifer, G. L. Williams, I. A. Vartaniants and I. K. Robinson, *Phys. Rev. B: Condens. Matter Mater. Phys.*, 2007, **76**, 115425.

35 V. A. Lubarda, *Mech. Mater.*, 2003, **35**, 53.

36 Yu. Rosenberg, V. Sh. Machavariani, A. Voronel, S. Garber, A. Rubshtein, A. I. Frenkel and E. A. Stern, *J. Phys.: Condens. Matter*, 2000, **12**, 8081.

37 M. Mavrikakis, B. Hammer and J. K. Norskov, *Phys. Rev. Lett.*, 1998, **81**, 2819.

38 J. Greeley, I. E. L. Stephens, A. S. Bondarenko, T. P. Johansson, H. A. Hansen, T. F. Jaramillo, J. Rossmeisl, I. Chorkendorff and J. K. Norskov, *Nat. Chem.*, 2009, **1**, 552; P. Stasser, S. Koh, T. Anniyev, J. Greeley, K. More, Ch. Yu, Z. Liu, S. Kaya, D. Nordlund, H. Ogasawara, M. F. Toney and A. Nilson, *Nat. Chem.*, 2010, **2**, 454.

39 Z. Tian, D. Sander, N. N. Negulyaev, V. S. Stepanyk and J. Kirschner, *Phys. Rev. B: Condens. Matter Mater. Phys.*, 2010, **81**, 113407.

40 Z. Q. Tian, B. Ren and D.-J. Wu, *J. Phys. Chem. B*, 2002, **106**, 9463.

41 A. Sun-Miguel, *Chem. Soc. Rev.*, 2006, **35**, 876.

42 N. Liu, L. Ming, L. Tang, M. Hentschel, H. Giessen and A. P. Alivisatos, *Nature*, 2011, **10**, 631.